The 8th European Congress on Computational Methods in Applied Sciences and Engineering
ECCOMAS Congress 2022
5-–9 June 2022, Oslo, Norway

DEVELOPMENT OF A DISCONTINUOUS GALERKIN SOLVER FOR THE SIMULATION OF TURBINE STAGES

A. Colombo[1], A. Ghidoni[2], E. Mantecca[2], G. Noventa[2], S. Rebay[2], D. Pasquale[3]

[1] University of Bergamo
Department of Engineering and Applied Sciences
viale Marconi 5, 24044 Dalmine (BG), Italy
e-mail: alessandro.colombo@unibg.it

[2] University of Brescia
Department of Mechanical and Industrial Engineering
via Branze 38, 25123 Brescia, Italy
email: (antonio.ghidoni,e.mantecca,gianmaria.noventa,stefano.rebay)@unibs.it

[3] Turboden S.p.A.
via Cernaia 10, 25124 Brescia, Italy
email: david.pasquale@turboden.it

Key words: Discontinuous Galerkin, Organic Rankine cycle, real gas, turbine stage

Abstract. A high-order Discontinuous Galerkin (DG) solver is assessed in the computation of the flow through an Organic Rankine Cycle turbine nozzle and stage. The flow features are predicted with a RANS (Reynolds averaged Navier–Stoke) approach and the k-log(ω) turbulence model in a multi reference frame, where interfaces between fixed and rotating zones are treated with a mixing plane approach, and non reflecting boundary conditions are used. Primitive variables based on pressure and temperature logarithms are adopted to ensure non-negative thermodynamic variables at a discrete level. The fluid can be modeled with the polytropic ideal gas law and the Peng-Robinson equation of state.

1 INTRODUCTION

In the last decades applications characterized by non-ideal compressible flows can be found in many industrial fields, such as Organic Rankine Cycle (ORC) turbomachinery. The working fluid (heavy hydrocarbons, fluorocarbons and siloxanes) for an ORC can show a non-ideal thermodynamic behaviour in the region where, for example, the expansion takes place, i.e. when pressure and temperatures are close to the liquid-vapour saturation curve in the region near the critical point. In these conditions the ideal gas law fails in predicting accurately the thermodynamic behaviour, and more complex equations of state are required, such as the Van der Waals or Peng-Robinson equations of state (EoS) or multi-parameter EoS.

To enhance the design of this family of turbomachinery, in recent years the coupling of accurate CFD tools with sophisticated thermodynamic models has been investigated, mainly for Finite Volume solvers. However, the increasing computational power, and the higher accuracy

expected by the design offices worldwide, motivate the recent interest in higher-order accurate methods, such as Discontinuous Galerkin (DG) methods. DG methods are particularly attractive for their geometrical flexibility [1], simple implementation of h/p adaptive techniques [2, 3], and compact stencil. Their drawback with respect to standard finite volume (FV) methods is the higher computation cost, which prevents a widespread application, and promotes many research efforts to devise more efficient computational approaches [4, 5].

In this work a high-order Discontinuous Galerkin (DG) solver [6, 7] is assessed in the computation of the flow through an Organic Rankine Cycle turbine nozzle and stage. The flow features are predicted with a RANS (Reynolds averaged Navier–Stoke) approach and the k-log(ω) turbulence model in a multi reference frame, where interfaces between fixed and rotating zones are treated with a mixing plane approach, and non reflecting boundary conditions [8]. Primitive variables based on pressure and temperature logarithms are adopted to ensure non-negative thermodynamic variables at a discrete level. The fluid can be modeled with the polytropic ideal gas law and the Peng-Robinson equation of state.

2 GOVERNING EQUATIONS

Governing equations can be written in the fixed and rotating frame as

$$\frac{\partial \rho}{\partial t} + \frac{\partial}{\partial x_j}(\rho u_{r,j}) = 0, \tag{1}$$

$$\frac{\partial}{\partial t}(\rho u_i) + \frac{\partial}{\partial x_j}(\rho u_{r,j} u_i) = -\frac{\partial p}{\partial x_i} - \rho s_{r,i} + \frac{\partial \widehat{\tau}_{ji}}{\partial x_j}, \tag{2}$$

$$\frac{\partial}{\partial t}(\rho E) + \frac{\partial}{\partial x_j}(\rho u_{r,j} H) = \frac{\partial}{\partial x_j}\left[u_i \widehat{\tau}_{ij} - \widehat{q}_j\right] - \tau_{ij}\frac{\partial u_i}{\partial x_j} + \beta^* \rho \overline{k} e^{\widetilde{\omega}_r}, \tag{3}$$

$$\frac{\partial}{\partial t}(\rho k) + \frac{\partial}{\partial x_j}(\rho u_{r,j} k) = \frac{\partial}{\partial x_j}\left[(\mu + \sigma^* \overline{\mu}_t)\frac{\partial k}{\partial x_j}\right] + \tau_{ij}\frac{\partial u_i}{\partial x_j} - \beta^* \rho \overline{k} e^{\widetilde{\omega}_r}, \tag{4}$$

$$\frac{\partial}{\partial t}(\rho \widetilde{\omega}) + \frac{\partial}{\partial x_j}(\rho u_{r,j} \widetilde{\omega}) = \frac{\partial}{\partial x_j}\left[(\mu + \sigma \overline{\mu}_t)\frac{\partial \widetilde{\omega}}{\partial x_j}\right] + \frac{\alpha}{\overline{k}}\tau_{ij}\frac{\partial u_i}{\partial x_j} - \beta \rho e^{\widetilde{\omega}_r} + (\mu + \sigma \overline{\mu}_t)\frac{\partial \widetilde{\omega}}{\partial x_k}\frac{\partial \widetilde{\omega}}{\partial x_k}, \tag{5}$$

where u_i can be the absolute ($u_{a,i}$) or the relative ($u_{r,i}$) velocity, depending on where the unknown variables are considered (fixed or rotating frame), and

$$E = \hat{e} + u_k u_k/2 - f_r(\epsilon_{ijk}\omega_i r_{c,j})(\epsilon_{ijk}\omega_i r_{c,j})/2, \tag{6}$$

$$H = h + u_k u_k/2 - f_r(\epsilon_{ijk}\omega_i r_{c,j})(\epsilon_{ijk}\omega_i r_{c,j})/2, \tag{7}$$

$$\tau_{ij} = 2\overline{\mu}_t\left[S_{ij} - \frac{1}{3}\frac{\partial u_k}{\partial x_k}\delta_{ij}\right] - \frac{2}{3}\rho \overline{k}\delta_{ij}, \tag{8}$$

$$\widehat{\tau}_{ij} = 2\mu\left[S_{ij} - \frac{1}{3}\frac{\partial u_k}{\partial x_k}\delta_{ij}\right] + \tau_{ij}, \tag{9}$$

$$\widehat{q}_j = -\left(\frac{\mu}{\mathrm{Pr}} + \frac{\overline{\mu}_t}{\mathrm{Pr}_t}\right)c_p\frac{\partial T}{\partial x_j}, \tag{10}$$

$$\overline{\mu}_t = \alpha^* \rho \overline{k} e^{-\widetilde{\omega}_r}, \quad \overline{k} = \max(0, k), \tag{11}$$

where $\hat{e}$ is the internal energy, h the enthalpy, ϵ_{ijk} the Levi-Civita tensor, Pr and Pr_t are the molecular and turbulent Prandtl numbers and

$$S_{ij} = \frac{1}{2}\left(\frac{\partial u_i}{\partial x_j} + \frac{\partial u_j}{\partial x_i}\right)$$

is the mean strain-rate tensor.

The source term components, $s_{r,i}$, include the Coriolis acceleration, $2\boldsymbol{\omega} \times \hat{\mathbf{u}}$, where $\hat{\mathbf{u}} = \mathbf{u}_r + f_r\,(\boldsymbol{\omega} \times \mathbf{r}_c)$, and the centripetal acceleration, $\boldsymbol{\omega} \times \boldsymbol{\omega} \times \mathbf{r}_c$, and are defined as

$$\mathbf{s}_r = \begin{pmatrix} \omega_2\hat{u}_3 - \omega_3\hat{u}_2 + \omega_2\left(\omega_1 r_{c,2} - \omega_2 r_{c,1}\right) - \omega_3\left(\omega_3 r_{c,1} - \omega_1 r_{c,3}\right) \\ \omega_3\hat{u}_1 - \omega_1\hat{u}_3 + \omega_3\left(\omega_2 r_{c,3} - \omega_3 r_{c,2}\right) - \omega_1\left(\omega_1 r_{c,2} - \omega_2 r_{c,1}\right) \\ \omega_1\hat{u}_2 - \omega_2\hat{u}_1 + \omega_1\left(\omega_3 r_{c,1} - \omega_1 r_{c,3}\right) - \omega_2\left(\omega_2 r_{c,3} - \omega_3 r_{c,2}\right) \end{pmatrix}. \tag{12}$$

If the unknown variables are considered in the fixed or rotating frame, the parameter f_r assumes the value 0 or 1, respectively.

The values of the closure parameters α,α^*, β, β^*, σ, σ^* can be found in [9]. The production term of the energy equation and the destruction term of the k and $\widetilde{\omega}$ equations are computed with the value $\widetilde{\omega}_r$, which satisfies the realizability condition for the turbulent stresses.

3 THERMODYNAMIC MODELS AND TRANSPORT PROPERTIES

In this work, the thermodynamic properties of the working fluid are modeled with two EoS that differ in complexity and accuracy: the polytropic ideal gas (PIG) and the Peng-Robinson [11] (PR) EoS.

The simplest thermodynamic model is the polytropic ideal gas model

$$p(\rho, T) = \rho R^* T, \tag{13}$$

where p denotes the pressure, T the temperature and ρ the density of the gas. $R^* = \mathcal{R}/M$, where $\mathcal{R} = 8314\ J/(mol\ K)$, is the universal gas constant and M is the molecular weight of the gas, while the ideal gas isochoric specific heat is given by the Mayer relation:

$$c_{v,ref} = c_{p,ref} - R^*. \tag{14}$$

Introducing the ratio of the isobaric to isochoric specific heat $\gamma = c_{p,ref}/c_{v,ref}$, polytropic behaviour (i.e., constant heat capacities) is granted by choosing a proper fixed reference value for $c_{v,ref}$. Due to the operating conditions, this value is set at the critical temperature T_{cr} as

$$c_{v,ref} = c_{p,0}(T_{cr}) - R^*, \tag{15}$$

where $c_{p,0}(T)$ is a polynomial function of the ideal gas isobaric specific heat given by

$$c_{p,0}(T) = A + BT + CT^2 + DT^3, \tag{16}$$

where A, B, C and D are substance dependent constant parameters calculated with the chemical group contribution method described in [20].

As a consequence, the ideal gas internal energy can be expressed as

$$e(T) = c_{v,ref}T = \frac{R^*T}{\gamma - 1}. \tag{17}$$

The Peng-Robinson EoS [11] is given by

$$p(\rho, T) = \frac{\rho R^* T}{1 - \rho b} - \frac{a\rho^2\alpha^2(T)}{1 + 2\rho b - \rho^2 b^2}, \tag{18}$$

where $\alpha(T)$ is a temperature dependent quantity, while a and b are constant parameters, which take into account molecular attraction forces and molecular volume, respectively. Their values are computed as

$$\alpha(T) = 1 + k\left(1 - \sqrt{\frac{T}{T_{cr}}}\right), \tag{19}$$

$$k = \begin{cases} 0.37464 + 1.54226\omega - 0.26992\omega^2 & if \quad \omega \leq 0.49 \\ 0.37964 + 1.48503\omega - 0.16442\omega^2 + 0.01667\omega^3 & if \quad \omega > 0.49 \end{cases}, \tag{20}$$

$$\omega = -\left(1 + log_{10}\left(\frac{p_{sat}}{p_{cr}}\right)_{\frac{T}{T_{cr}}=0.7}\right), \tag{21}$$

$$a = 0.45724\frac{(R^*T_{cr})^2}{p_{cr}}, b = 0.07780\frac{R^*T_{cr}}{p_{cr}}, \tag{22}$$

where p_{cr} is the critical pressure, p_{sat} is the saturation pressure and ω is the acentric factor, a constant parameter that estimates the non-sphericity of molecules.
The real gas internal energy is defined with the general relation [19]:

$$e(\rho, T) = \int_0^T c_{v,0}(T)dT + \int_0^\rho \frac{1}{\rho^2}\left[p - T\left(\frac{\partial p}{\partial T}\right)_\rho\right]d\rho, \tag{23}$$

where the ideal gas contribution to the isochoric specific heat is given by

$$c_{v,0}(T) = c_{v,0}(T_{cr})\left(\frac{T}{T_{cr}}\right)^n, \tag{24}$$

as suggested in [18] to simplify calculations. The exponent n is a constant and is defined as

$$n = \frac{ln\left(c_{v,0}(T_2)/c_{v,0}(T_1)\right)}{ln\left(T_2/T_1\right)}, \tag{25}$$

where T_1 and T_2 satisfy the following constraint: $T_1 < T_{cr} < T_2$. The quantities $c_{v,0}(T_{cr})$, $c_{v,0}(T_1)$ and $c_{v,0}(T_2)$ are evaluated by the polynomial law for the isobaric specific heat as $c_{v,0}(T) = c_{p,0}(T) - R^*$.

The internal energy, according to Peng-Robinson EoS, can be written as

$$e(\rho, T) = \int_0^T c_{v,0}(T)dT - \frac{a}{b}\frac{(k+1)\alpha(T)}{\sqrt{2}}atanh\left(\frac{\sqrt{2}\rho b}{1 + \rho b}\right), \tag{26}$$

while the real gas isochoric and isobaric specific heats are defined through two general relations [17]:

$$c_v(\rho,T) = \left(\frac{\partial e}{\partial T}\right)_\rho = c_{v,0}(T) - T\int_0^\rho \frac{1}{\rho^2}\left(\frac{\partial^2 p}{\partial T^2}\right)_\rho d\rho, \tag{27}$$

$$c_p(\rho,T) = c_v(\rho,T) + \frac{T}{\rho^2}\frac{\left(\frac{\partial p}{\partial T}\right)^2_\rho}{\left(\frac{\partial p}{\partial \rho}\right)_T}. \tag{28}$$

The dynamic viscosity μ is also computed with a power law that approximates its variation with the temperature

$$\frac{\mu}{\mu_{ref}} = \left(\frac{T}{T_{ref}}\right)^\beta, \tag{29}$$

where μ_{ref} and T_{ref} are reference values, and the exponent β is a constant parameter. By assuming a constant Prandtl number Pr, the thermal conductivity can be computed from the viscosity as $\kappa(\rho,T) = c_p(\rho,T)\mu/Pr$.

4 DISCONTINUOUS GALERKIN DISCRETIZATION

Governing equations can be written in compact form as

$$\mathbf{P}(\mathbf{w})\frac{\partial \mathbf{w}}{\partial t} + \nabla\cdot\mathbf{F}_c(\mathbf{w}) + \nabla\cdot\mathbf{F}_v(\mathbf{w},\nabla\mathbf{w}) + \mathbf{s}(\mathbf{w},\nabla\mathbf{w}) = \mathbf{0}, \tag{30}$$

where $\mathbf{w}$ is the unknown vector, $\mathbf{F}_c$ and $\mathbf{F}_v$ are the convective and viscous flux functions, $\mathbf{s}$ the vector of source terms. $\mathbf{w} = \left[\widetilde{p}, u_1, u_2, u_3, \widetilde{T}, k, \widetilde{\omega}\right]^T$ is the unknown vector, where the polynomial approximation of the working variables $\widetilde{p} = \log(p)$ and $\widetilde{T} = \log(T)$ are used (see [12] for details). Notice that the use of $\widetilde{p}$ and $\widetilde{T}$ does not modify the governing equations.

The governing equations are discretized in space by multiplying the system (30) with an arbitrary smooth test function $\mathbf{v} = \{v_1,\ldots,v_m\}$ and integrating by parts. The solution and the test function are replaced with a finite element approximation $\mathbf{w}_h$ and a discrete test function $\mathbf{v}_h$ that belong to the discrete polynomial space in physical coordinates $\mathbf{V}_h \stackrel{\text{def}}{=} [\mathbb{P}^k_d(\mathcal{T}_h)]^m$.

The set of test and shape functions in any element K is chosen coincident with the set $\{\phi\}$ of N^K_{dof} orthogonal and hierarchical basis functions in that element.

Each component $w_{h,j}$, $j = 1,\ldots,m$, of the numerical solution $\mathbf{w}_h \in \mathbf{V}_h$ can be expressed as $w_{h,j} = \phi_l W_{j,l}$, $l = 1,\ldots,N^K_{dof}$, $\forall K \in \mathcal{T}_h$.

The DG discretization of the governing equations consists in seeking, for $j = 1,\ldots,m$, the elements of $\mathbf{W}$ such that

$$\begin{aligned}\sum_{K\in\mathcal{T}_h}\int_K \phi_i P_{j,k}\left(\mathbf{w}_h\right)\phi_l\frac{dW_{k,l}}{dt}d\mathbf{x} - \sum_{K\in\mathcal{T}_h}\int_K \frac{\partial\phi_i}{\partial x_n}F_{j,n}\left(\mathbf{w}_h,\nabla_h\mathbf{w}_h + \mathbf{r}\left(\llbracket\mathbf{w}_h\rrbracket\right)\right)d\mathbf{x}\\ + \sum_{F\in\mathcal{F}_h}\int_F \llbracket\phi_i\rrbracket_n\,\widehat{F}_{j,n}\left(\mathbf{w}_h^{\pm},\left(\nabla_h\mathbf{w}_h + \eta_F\mathbf{r}_F\left(\llbracket\mathbf{w}_h\rrbracket\right)\right)^{\pm}\right)d\sigma\\ + \sum_{K\in\mathcal{T}_h}\int_K \phi_i s_j\left(\mathbf{w}_h,\nabla_h\mathbf{w}_h + \mathbf{r}\left(\llbracket\mathbf{w}_h\rrbracket\right)\right)d\mathbf{x} = 0,\end{aligned} \tag{31}$$

for $i = 1, \ldots, N_{dof}^K$. $F_{j,n}$ is the sum of the convective and viscous flux functions. As the functional approximation is discontinuous, the flux is not uniquely defined, a numerical flux vector, $\widehat{F}_{j,n}$, over the mesh faces is adopted. The convective part is based on the solution of local Riemann problems with the approximate Riemann solver of Roe [13], generalized to the case of an arbitrary EoS following the Vinokur-Montagné approach [14], while the viscous part is discretized with the BR2 scheme [15].

The shock-capturing technique adopted in this work is based on the approach presented in [1], and inside each element is introduced an artificial diffusion contribution, without using any shock sensor to detect discontinuities. The shock-capturing term is always active, but, only a numerical viscosity is introduced only in regions where unphysical oscillations are present.

By numerically computing the integrals in Eq. (31), the following ODEs system is obtained:

$$\mathbf{M_P}\left(\mathbf{W}\right)\frac{d\mathbf{W}}{dt} + \mathbf{R}\left(\mathbf{W}\right) = \mathbf{0}, \tag{32}$$

where $\mathbf{R}\left(\mathbf{W}\right)$ is the vector of residuals and $\mathbf{M_P}\left(\mathbf{W}\right)$ is the global block diagonal matrix arising from the discretization of the first integral in Eq. (31). The linearized backward Euler scheme with a pseudo-transient continuation strategy is adopted for the time integration, and the linear system is solved using the restarted GMRES algorithm, as available in the PETSc library [16].

4.1 Mixing plane and non reflecting boundary conditions

The mixing-plane interface allows to perform steady state calculations, coupling the fixed (stator) and the rotating (rotor) domains, where equations are solved with a multi reference frame approach. It removes the dependency of the results on the relative position between the rotor and the stator. Outlet (upstream domain) and inlet (downstream domain) are averaged in the pitch-wise direction, and mixed-out average is used to guarantee the conservation of mass, momentum and energy.

In turbomachinery applications both the outflow and inflow boundary conditions are set really close to the blades, and a small space exists between rotor and stator rows. Standard inflow/outflow boundary conditions lead to the appearance of fictitious reflections that compromise the accuracy of the solution. A set of boundary conditions that correctly describes the incoming waves is thus required to avoid spurious oscillations of the solution. Giles [8] non reflecting boundary conditions (NRBC) are chosen. NRBC decomposes the flow into its average component (user specified/Mixing-plane quantities), and the fluctuating component, which is obtained by means of a Fourier decomposition. The fluctuating component of the incoming waves is treated according to the exact two-dimensional theory and prevent spurious reflections at the boundary.

5 RESULTS

The MIGALE code is used to investigate the real gas flow for a sub-critical expansion through the *i*) nozzle and the *ii*) first stage of an ORC turbine. The influence of the thermodynamic models on the predicted aerodynamic performance is investigated. The MDM siloxane is considered as working fluid, which is characterized by a high molecular weight $M = 236.5315\ g/mol$. The constant ratio of specific heats is set to $\gamma = 1.0173346$ for the PIG model. A $\mathbb{P}^2$ polynomial

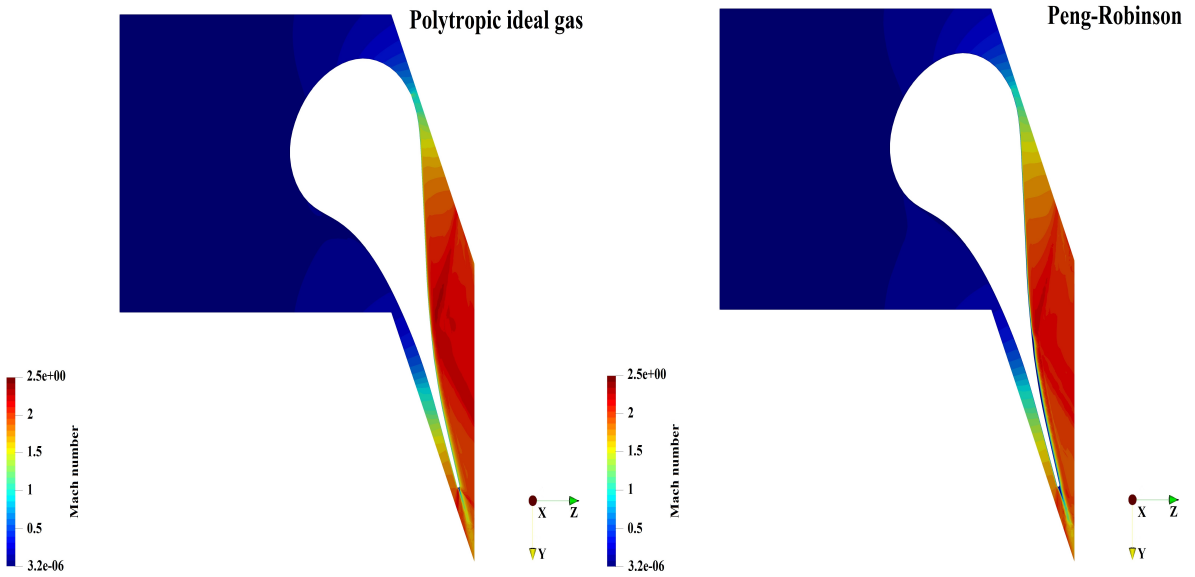

Figure 1: Mach number contours for PIG (left) and PR (right) EoS. $\mathbb{P}^2$ solution approximation

solution approximation has been adopted for both computations. The L^2 norm of all residuals ($|res_i|_{L^2} < 10^{-6},\ i = 1, \ldots, 7$) has been used as a convergence indicator.

5.1 ORC turbine Nozzle

The mesh consists of 5128 quadratic elements, hexahedra in the boundary layer and prisms outside. The height of elements adjacent to the solid wall corresponds to a $y^+ \approx 5$. At the inflow, the total pressure, $p_{01} = 8\ bar$, total temperature, $T_{01} = 545\ K$, flow angle, $\alpha_1 = 0°$, turbulence intensity, $Tu_1 = 4\%$, and viscosity ratio, $(\mu_t/\mu)_1 = 10$, are prescribed. At the outflow, the static pressure is set equal to $p_2 = 0.96\ bar$.

Figure 1 compares the Mach number contours obtained with PIG and PR models. The predicted flow fields are slightly affected by PR and PIG models, even if some differences are evident. This can be ascribed to the compressibility factor, $Z = pv/(R^*T)$, which is around $Z_1 = 0.71$ at the beginning of the expansion and is close to the unitary value of the PIG model near the outflow.

5.2 ORC turbine stage

The mesh consists of 10963 quadratic elements, hexahedra in the boundary layer and prisms outside. The height of elements adjacent to the solid wall corresponds to a $y^+ \approx 5$. At the inflow, the total pressure, $p_{01} = 9.11\ bar$, total temperature, $T_{01} = 535\ K$, flow angle, $\alpha_1 = 0°$, turbulence intensity, $Tu_1 = 4\%$, and viscosity ratio, $(\mu_t/\mu)_1 = 10$, are prescribed. At the outflow, the static pressure is seto equal to $p_2 = 1\ bar$. The rotational speed of the rotor is set equal to $\boldsymbol{\omega} = [0, 0, 314.16\ rad/s]^T$.

Also in this case, even if the compressibility factor at the beginning of the expansion is slightly lower, $Z_1 = 0.66$, the predicted Mach number contours (see Fig. 2) are not heavily affected by

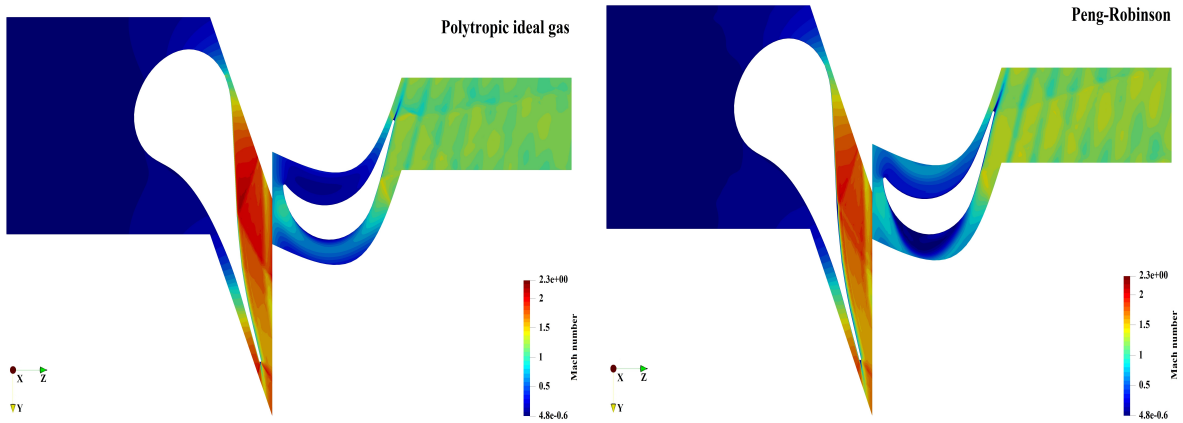

Figure 2: Mach number contours for PIG (left) and PR (right) EoS. $\mathbb{P}^2$ solution approximation

the chosen thermodynamic model. The effect of the different fluid models are more evident on the density and speed of sound distributions on the stator and rotor blades, as shown in Fig. 3.

6 CONCLUSIONS

The MIGALE code, recently extended to the solution of turbomachinery stages, has been used to investigate the expansion from subcritical inlet conditions through an ORC turbine nozzle and stage. The computations have been performed with two fluid models of increasing complexity and accuracy, i.e. PIG and PR models. The computations clearly show that the simple polytropic ideal gas model is not suited for the simulation of the flow through the investigated ORC applications, and a more accurate model must be used. Moreover, Giles mixing plane and NRBC are able to couple stator and rotor avoiding nonphysical oscillation, also in a high order context.

Future work will be devoted to the implementation in the code of more complex models for transport properties and to the assessment of the solver on more complex 3D configurations.

REFERENCES

[1] Bassi, F. and Botti, L. and Colombo, A. and Crivellini, A. and Franchina, N. and Ghidoni, A. and Rebay, S. Very High-Order Accurate Discontinuous Galerkin Computation of Transonic Turbulent Flows on Aeronautical Configurations. *ADIGMA - A European Initiative on the Development of Adaptive Higher-Order Variational Methods for Aerospace Applications* of *Notes on Numerical Fluid Mechanics and Multidisciplinary Design* (2010) **113**:25–38.

[2] Bassi, F. and Colombo, A. and Crivellini, A. and Fidkowski, K.J. and Franciolini, M. and Ghidoni, A. and Noventa, G. An entropy-adjoint p-adaptive discontinuous Galerkin method for the under-resolved simulation of turbulent flows. *AIAA Aviation 2019 Forum* (2019) 1–17.

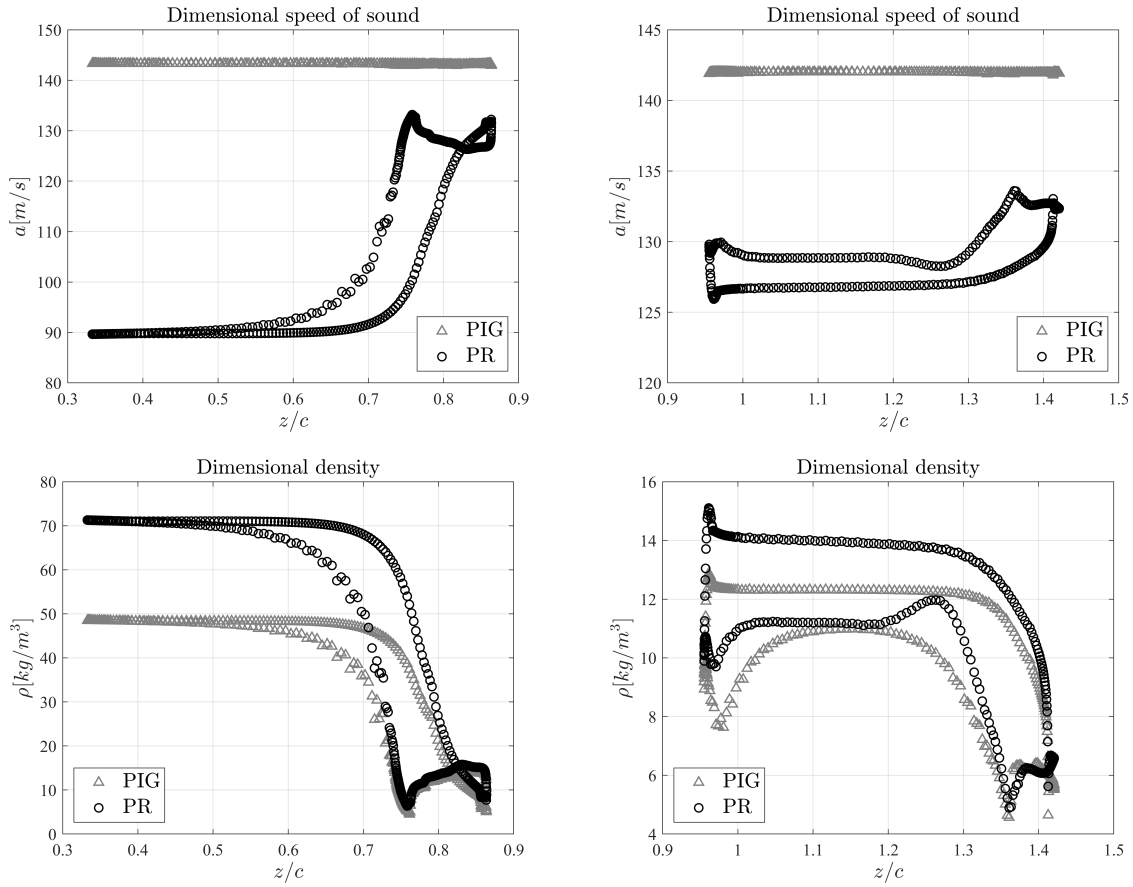

Figure 3: Speed of sound (top) and density (bottom) for stator (left) and rotor (right). $\mathbb{P}^2$ solution approximation

[3] Bassi, F. and Colombo, A. and Crivellini, A. and Fidkowski, K.J. and Franciolini, M. and Ghidoni, A. and Noventa, G. Entropy-adjoint p-adaptive discontinuous Galerkin method for the under-resolved simulation of turbulent flows. *AIAA Journal* (2020) **58**:3963–3977.

[4] Bassi, F. and Ghidoni, A. and Rebay, S. Optimal Runge-Kutta smoothers for the p-multigrid discontinuous Galerkin solution of the 1D Euler equations. *Journal of Computational Physics* (2011) **230**:4153–4175.

[5] Colombo, A. and Ghidoni, A. and Noventa, G. and Rebay, S. p-Multigrid High-Order Discontinuous Galerkin Solution of Compressible Flows. *CISM International Centre for Mechanical Sciences* (2021) `https://doi.org/10.1007/978-3-030-60610-7_4`.

[6] Bassi, F. and Botti, L. and Colombo, A. and Crivellini, A. and De Bartolo, C. and Franchina, N. and Ghidoni, A. and Rebay, S. Time integration in the discontinuous Galerkin code MIGALE – Steady problems. *Notes on Numerical Fluid Mechanics and Multidisciplinary Design* (2015) **128**:179–204.

[7] Bassi, F. and Botti, L. and Colombo, A. and Crivellini, A. and Franchina, N. and Ghidoni, A. Assessment of a high-order accurate Discontinuous Galerkin method for turbomachinery flows. *International Journal of Computational Fluid Dynamics* (2016) **30**:307–328.

[8] Saxer, A.P. and Giles, M.B. Quasi-three-dimensional nonreflecting boundary conditions for Euler equations calculations. *Journal of Propulsion and Power*, (1993) **9**:263–271.

[9] Wilcox, D. C. *Turbulence Modelling for CFD*. La Cañada, CA 91011, USA: DCW industries Inc, (2006)

[10] Bassi, F. and Crivellini, A. and Rebay, S. and Savini, M. Discontinuous Galerkin Solution of the Reynolds-Averaged Navier-Stokes and k-ω turbulence model equations. *Comput. Fluids* (2005) **34**:507–540.

[11] Peng, D.Y. and Robinson, D.B. A New Two-Constant Equation of State *Ind. Eng. Chem. Fundam.* (1976) **15**:59–64.

[12] Bassi, F. and Botti, L. and Colombo, A. and Ghidoni, A. and Massa, F. Linearly implicit Rosenbrock-type Runge–Kutta schemes applied to the Discontinuous Galerkin solution of compressible and incompressible unsteady flows. *Comput. Fluids* (2015) **118**:305–320.

[13] Roe, P.L. Approximate Riemann solvers, parameter vectors and difference schemes. *Journal of Computational Physics* (1981) **43**:357–372.

[14] Vinokur, M. and Montagné J.M. Generalized flux-vector splitting and Roe average for an equilibrium real gas. *J. Comput. Phys.* (1990) **89**:276–300.

[15] Bassi, F. and Rebay, S. and Mariotti, G. and Pedinotti, S. and Savini, M. A high-order accurate discontinuous finite element method for inviscid and viscous turbomachinery flows. In *Proceedings of the 2nd European Conference on Turbomachinery Fluid Dynamics and Thermodynamics* edited by R. Decuypere and G. Dibelius (1997) 99–108.

[16] Balay, S. and Adams, M.F. and Brown, J. and Brune, P. and Buschelman, K. and Eijkhout, V. and Gropp, W.D. et al. PETSc Web page. (2014) `http://www.mcs.anl.gov/petsc`.

[17] Hanimann, L. and Mangani, L. and Casartelli, E. and Vogt, D.M. and Darwish, M. Real Gas Models in Coupled Algorithms Numerical Recipes and Thermophysical Relations. *Int. J. Turbomach. Propuls. Power* (2020) **5**.

[18] Cramer, M.S. Negative nonlinearity in selected fluorocarbons. *Physics of Fluids A: Fluid Dynamics* (1989) **1**:1894-1897.

[19] Reynolds W.C. Thermodynamic properties in SI: Graphs, tables, and computational equations for forty substances. *Stanford University, Department of Mechanical Engineering* (1979).

[20] Poling, B.E. and Prausnitz, J.M. and O'Connell, J.P. The Properties of Gases and Liquids 5E. *McGraw-Hill Education* (2000).